crystals

MDPI

Article

Synthesis and Crystallographic Characterisation of Pyridyl- and Indoleninyl-Substituted Pyrimido[1,2-b]indazoles

Abdul Qaiyum Ramle [1,*], Sang Loon Tan [2,*] and Edward R. T. Tiekink [2,*]

[1] School of Chemical Sciences, Universiti Sains Malaysia (USM), Penang 11800, Malaysia
[2] Research Centre for Crystalline Materials, School of Medical and Life Sciences, Sunway University, Bandar Sunway 47500, Malaysia
* Correspondence: qaiyum@usm.my (A.Q.R.); alant@sunway.edu.my (S.L.T.); edwardt@sunway.edu.my (E.R.T.T.); Tel.: +60-3-7491-7181(E.R.T.T.)

Abstract: Pyridyl- and indoleninyl-substituted pyrimido[1,2-*b*]indazole were synthesised in good to high yields from the condensation reaction of 1,3-dialdehydes with 3-aminoindazoles. The structural features of the compounds were determined by NMR (^{1}H, ^{13}C and ^{19}F), FT-IR and HR-MS. The spectroscopic assignments were confirmed by X-ray crystallography for two derivatives, i.e., 9-Bromo-3-(pyridin-4-yl)pyrimido[1,2-b]indazole (**1b**) and 10-Methoxy-3-(pyridin-4-yl)pyrimido[1,2-b]indazole (**1c**), which further provides support for significant delocalisation of π-electron density over the entire fused ring system. The molecular packing was assessed by conventional methods together with Hirshfeld surface analyses. In **1b**, the molecular packing features pyrimidyl-N–H···N(pyrimidyl), π(pyrazolyl)···π(pyrimidyl) and Br···N interactions within a two-dimensional array. In **1c**, pyrimidyl-C–H···N(pyrazolyl) and pyridyl-C–H···O(methoxy) interactions feature within a three-dimensional architecture.

Keywords: 1,3-dialdehydes; 3-aminoindazoles; condensation reaction; pyrimido[1,2-*b*]indazole

Citation: Ramle, A.Q.; Tan, S.L.; Tiekink, E.R.T. Synthesis and Crystallographic Characterisation of Pyridyl- and Indoleninyl-Substituted Pyrimido[1,2-b]Indazoles. *Crystals* **2022**, *12*, 1283. https://doi.org/10.3390/cryst12091283

Academic Editor: Sławomir Grabowski

Received: 24 August 2022
Accepted: 2 September 2022
Published: 9 September 2022

Publisher's Note: MDPI stays neutral with regard to jurisdictional claims in published maps and institutional affiliations.

Copyright: © 2022 by the authors. Licensee MDPI, Basel, Switzerland. This article is an open access article distributed under the terms and conditions of the Creative Commons Attribution (CC BY) license (https://creativecommons.org/licenses/by/4.0/).

1. Introduction

Nitrogen-fused tricyclic frameworks are frequently found in a diverse range of naturally occurring products and synthetic drugs [1,2]. The nitrogen-rich structural core plays an important role in numerous biological activities such as anti-cancer [3], anti-inflammatory [4], monoamine oxidase (MOA) [5], PDE10A inhibitors [6], anti-anxiety [7], anti-malarial [8], anti-microbial [9] and are effective against the hepatitis C virus (HCV) infection [1]. Interestingly, some derivatives have been clinically used for the treatment of various ailment diseases [10]. The incorporation of the extended π-conjugation substituents alters the chromophore of the core which displays interesting photophysical and fluorescent properties in solution [11]. Despite the achievements in numerous fields, less effort has focused upon the preparation of pyrimido[1,2-*b*]indazole derivatives due to the low availability of appropriate starting materials, poor synthetic options and lack of functional group tolerance [1,12]. Hence, an efficient synthetic methodology to functionalise and extend the range of nitrogen-fused tricyclic frameworks is highly desirable.

A literature survey revealed that several research groups have reported a facile synthetic approach to synthesise the pyrimido[1,2-*b*]indazole core in recent years. Most strategies involve the condensation of 3-aminoindazoles with carbonyl groups to deliver a diverse range of pyrimido[1,2-*b*]indazole analogues [11,13–22]. Among those strategies, Gao et al. [2] reported the core can be achieved from the three-component reaction of 3-aminoindazoles, aromatic aldehydes and triethylamine in the presence of ammonium iodide (Scheme 1a). However, the method only decorated the core with a broad range of phenyl moieties at the C4-position. Furthermore, a straightforward and low-cost technique to

synthesise the core was described by Abarbi et al. [5] through a condensation of 3-aminoindazoles with 2-bromomalonaldehyde in the presence of catalytic acetic acid to afford the products in high yields (Scheme 1b). The synthetic approach was further utilised by Ramle et al. [23] to furnish the C-3 position of the core with a wide scope of indolenine substituents. Recently, Cao et al. [12] reported an efficient protocol to decorate the C2-position of the core with a variety of electronic substituents from the reaction between 3-aminoindazoles and ynals in the presence of ammonium thiocyanate under blue light-emitting diode (LED) irradiation (Scheme 1c). It is noted that the regioselective synthesis of pyrimido[1,2-*b*]indazole is due to the actions of both the reactants and the conditions used in the synthetic media, which involves a specific synthetic mechanism for the formation of the products.

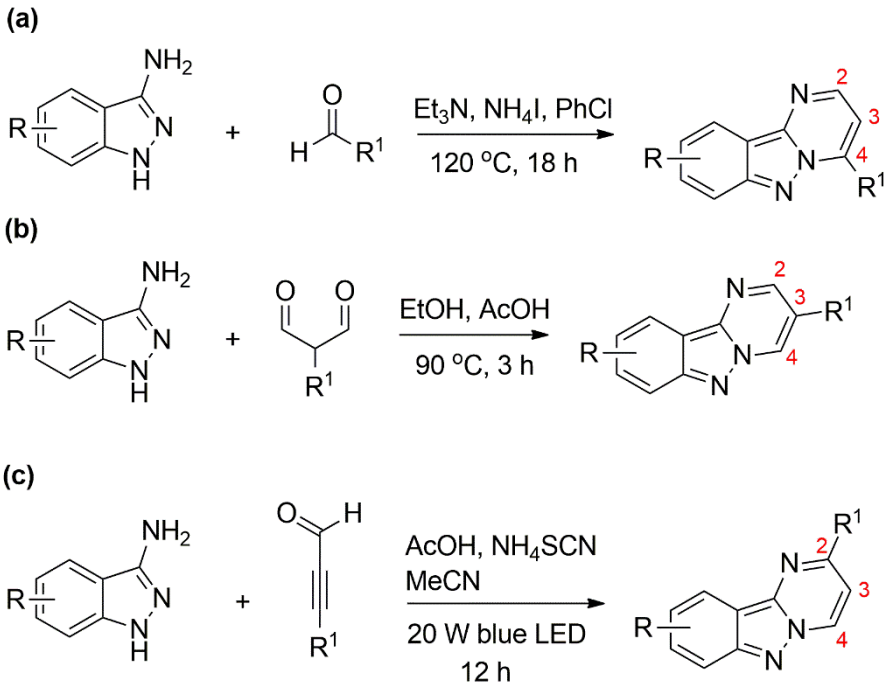

Scheme 1. (**a**–**c**) Examples of regioselective synthesis of substituted pyrimido[1,2-*b*]indazoles.

As part of continuing interest in this area, this article describes the preparation of two new series of pyrimido[1,2-*b*]indazoles containing pyridine and indolenine moieties via a simple and direct approach. The structural identity was physically characterised by various spectroscopic methods and complemented by X-ray crystallography on two derivatives. The outcomes of these investigations are reported herein.

2. Materials and Methods

2.1. Chemicals and Instrumentation

All chemicals and solvents were purchased from Fischer Scientific, Merck Millipore, and Sigma Aldrich, Malaysia. ^{1}H and ^{13}C NMR spectra were recorded on a JEOL ECX 400 MHz (JEOL Ltd., Tokyo, Japan), Bruker DMX 400 MHz (BRUKER Corporation, Massachusetts, USA) and Bruker DMX 600 MHz (BRUKER Corporation, Massachusetts, USA) instruments; the ^{19}F NMR spectra of **1d** and **4d** (Supplementary Materials) were measured on JEOL ECX 400 MHz and BRUKER DMX 400 MHz instruments, respectively. The chemical shifts (δ) and coupling constant (J) values are expressed in terms of ppm and Hz units, respectively. FT-IR spectra were collected on an ATR-FT-IR Perkin Elmer Spectrum 400 IR spectrophotometer (PerkinElmer Inc, Waltham, USA). An Agilent 6530 Accurate-Mass Q-TOF LC/MS instrument (Agilent Technologies Inc, Santa Clara, CA, USA) was used to

obtain the LCMS spectra. Melting points were recorded on a Mel-Temp II (American Laboratory Trading, San Diego, CA, USA).

2.2. Synthetic Procedure for the Preparation of **1a–d**

A mixture of 2-(4-pyridinyl)malonaldehyde (0.5 mmol, 1 equiv.) and 3-aminoindazoles (0.5 mmol, 1 equiv.) in EtOH/AcOH (*v*/*v* = 4:1, 5 mL) was heated at 78 °C for 4 h. Upon completion, the reaction was cooled to room temperature. The solid was filtered, washed with diethyl ether (50 mL) and dried at 60 °C for several hours to afford the pure product.

3-(Pyridin-4-yl)pyrimido[1,2-b]indazole (**1a**): Yellow solid. Yield: 55%. mp: 246–248 °C. ^{1}H NMR (400 MHz, DMSO-d_6): δ = 10.00 (d, 1H, *J* = 2.0 Hz, CHN), 9.24 (d, 1H, *J* = 1.6 Hz, CHN), 8.77 (d, 2H, *J* = 6.4 Hz, Ar-H), 8.31 (d, 1H, *J* = 8.0 Hz, Ar-H), 8.05 (d, 2H, *J* = 8.0 Hz, Ar-H), 7.87 (d, 1H, *J* = 8.8 Hz, Ar-H), 7.70 (t, 1H, *J* = 5.2 Hz, Ar-H), 7.38 (t, 1H, *J* = 7.6 Hz, Ar-H). ^{13}C NMR (150 MHz, DMSO-d_6): δ = 151.29, 150.44, 145.02, 142.46, 140.96, 132.69, 130.05, 122.53, 121.59, 121.11, 120.49, 116.09, 112.51. FT-IR (ATR): ν 3036 (C-H), 1637, 1602, (C=N pyridine), 1591, 1551 (C=C), 1223 (C-N) cm^{-1}. HRMS (ESI): *m*/*z* [M+H]$^{+}$ calcd. for $C_{15}H_{11}N_4$: 247.0978; found: 247.0850.

9-Bromo-3-(pyridin-4-yl)pyrimido[1,2-b]indazole (**1b**): Yellow solid. Yield: 60%. mp: 254–256 °C. ^{1}H NMR (600 MHz, DMSO-d_6): δ = 10.02 (d, 1H, *J* = 2.4 Hz, CHN), 9.29 (d, 1H, *J* = 1.8 Hz, CHN), 8.78 (dd, 2H, *J* = 6.0, 3.0 Hz, Ar-H), 8.49 (d, 1H, *J* = 1.8 Hz, Ar-H), 8.05 (dd, 2H, *J* = 6.0, 3.0 Hz, Ar-H), 7.87 (d, 1H, *J* = 9.6 Hz, Ar-H), 7.78 (dd, 1H, *J* = 9.0, 1.8 Hz, Ar-H). ^{13}C NMR (150 MHz, DMSO-d_6): δ = 150.95, 150.08, 146.42, 142.22, 141.23, 133.59, 133.49, 123.67, 123.03, 122.15, 118.94, 114.32, 113.67. FT-IR (ATR): ν 3054 (C-H), 1633, 1591 (C=N pyridine), 1554 (C=C), 1166 (C-N) cm^{-1}. HRMS (ESI): *m*/*z* [M+H]$^{+}$ calcd. for $C_{15}H_{10}N_4Br$: 326.9089; found: 326.9909. X-ray quality crystals were grown from a toluene solution after five days.

10-Methoxy-3-(pyridin-4-yl)pyrimido[1,2-b]indazole (**1c**): Yellow solid. Yield: 59%. mp: 230–232 °C. ^{1}H NMR (400 MHz, DMSO-d_6): δ = 9.95 (d, 1H, *J* = 2.4 Hz, CHN), 9.22 (d, 1H, *J* = 2.4 Hz, CHN), 8.77 (dd, 2H, *J* = 6.4, 2.8 Hz, Ar-H), 8.03 (dd, 2H, *J* = 6.0, 2.8 Hz, Ar-H), 7.61 (t, 1H, *J* = 8.4 Hz, Ar-H), 7.39 (d, 1H, *J* = 8.8 Hz, Ar-H), 6.74 (d, 1H, *J* = 7.6 Hz, Ar-H), 4.04 (s, 3H, OCH_3). ^{13}C NMR (150 MHz, DMSO-d_6): δ = 155.79, 153.34, 150.93, 145.67, 142.52, 141.47, 132.78, 131.60, 122.22, 121.99, 108.53, 104.60, 100.06, 56.04. FT-IR (ATR): ν 3045 (C-H), 1637, 1593 (C=N), 1567, 1506 (C=C), 1102 (C-N) cm^{-1}. HRMS (ESI): *m*/*z* [M+H]$^{+}$ calcd. for $C_{16}H_{13}N_4O$: 277.1084; found: 277.0942. X-ray quality crystals were grown from a toluene solution after five days.

3-(Pyridin-4-yl)-8-(trifluoromethyl)pyrimido[1,2-b]indazole (**1d**): Yellow solid. Yield: 60%. mp: 215–216 °C. ^{1}H NMR (600 MHz, DMSO-d_6): δ = 10.08 (d, 1H, *J* = 1.8 Hz, CHN), 9.33 (d, 1H, *J* = 1.8 Hz, CHN), 8.78 (dd, 2H, *J* = 6.0, 3.0 Hz, Ar-H), 8.51 (d, 1H, *J* = 8.4 Hz, Ar-H), 8.28 (s, 1H, Ar-H), 8.05 (dd, 2H, *J* = 6.0, 3.0 Hz, Ar-H), 7.56 (dd, 1H, *J* = 8.4, 1.2 Hz, Ar-H). ^{13}C NMR (150 MHz, DMSO-d_6): δ = 172.47, 150.95, 150.09, 146.98, 142.91, 141.04, 133.77, 130.62 (q, *J* = 30.6 Hz), 127.56 (q, *J* = 271.2 Hz), 124.18, 123.03, 122.18, 116.69 (q, *J* = 3.3 Hz), 114.75 (q, *J* = 4.4 Hz). ^{19}F NMR (376 MHz, DMSO-d_6): δ = −60.57. FT-IR (ATR): ν 3060 (C-H), 1648, 1595 (C=N), 1505 (C=C), 1122 (C-N) cm^{-1}. HRMS (ESI): *m*/*z* [M+H]$^{+}$ calcd. for $C_{16}H_{10}N_4F_3$: 315.0856; found: 315.0701.

2.3. Synthetic Procedure for the Preparation of **3**

To a solution of **1** (1.0 mmol, 1 equiv.) in MeOH/water (*v*/*v* = 1:1, 10 mL) was added 0.5 M NaOH (8 mL, 4 equiv.). The mixture of stirred vigorously at room temperature for 12 h (monitored by TLC). After completion of the reaction, the mixture was diluted with ethyl acetate (10 mL) and water (10 mL). The aqueous phase was collected and acidified to pH 4 by adding 0.1 M HCl. The resulting product was filtered, washed with water (50 mL) and dried at 60 °C to give the pure product.

2-(1,3-Dioxopropan-2-ylidene)-3,3-dimethylindoline-5-carboxylic acid (**3**): Yellow solid. Yield: 68%. mp: 279–278 °C. ^{1}H NMR (400 MHz, DMSO-d_6): δ = 13.11 (br, 1H, NH), 9.81 (s,

2H, CHO), 8.01 (d, 1H, *J* = 0.8 Hz, Ar-H), 7.89 (dd, 1H, *J* = 8.4, 1.6 Hz, Ar-H), 7.63 (d, 1H, *J* = 8.0 Hz, Ar-H), 1.65 (s, 6H, CH_3). ^{13}C NMR (100 MHz, DMSO-d_6): δ = 191.44, 188.76, 178.57, 167.53, 144.53, 140.94, 130.69, 127.88, 123.67, 114.15, 110.13, 50.76, 24.29. FT-IR (ATR): ν 3191, 3060, 2874, 2340, 1706 (C=O aldehyde), 1654 (C=O acid), 1609 (C=C) cm^{-1}. HRMS (ESI): *m*/*z* [M−H]$^-$ calcd. for $C_{14}H_{12}NO_4$: 258.0772; found: 258.0771.

2.4. General Procedure for the Preparation of **4a–d**

A mixture of **3** (0.15 mmol, 1 equiv.) and 3-aminoindazoles (0.15 mmol, 1.0 equiv.) in EtOH/AcOH (*v*/*v* = 4:1, 5 mL) was heated at 78 °C for 4 h. After cooling to room temperature, the solid was filtered, washed with EtOH (25 mL) and dried at 60 °C for several hours to afford the pure product.

3,3-Dimethyl-2-(pyrimido[1,2-b]indazol-3-yl)-3H-indole-5-carboxylic acid (**4a**): Yellow solid. Yield: 85%. mp: >300 °C. ^{1}H NMR (400 MHz, DMSO-d_6): δ = 10.00 (d, 1H, *J* = 2.0 Hz, CHN), 9.53 (d, 1H, *J* = 2.0 Hz, CHN), 8.31 (d, 1H, *J* = 8.4 Hz, Ar-H), 8.18 (s, 1H, Ar-H), 8.05 (dd, 1H, *J* = 8.0, 1.6 Hz, Ar-H), 7.89 (d, 1H, *J* = 8.8 Hz, Ar-H), 7.82 (m, 1H, Ar-H), 7.72 (m, 1H, Ar-H), 7.39 (m, 1H, Ar-H), 1.70 (s, 6H, CH_3). ^{13}C NMR (100 MHz, DMSO-d_6): δ = 182.18 (C=N indole), 167.83 (C=O), 156.32, 152.26, 148.35, 146.21, 143.10, 134.83, 130.97, 130.48, 129.34, 123.25, 122.10, 121.21, 121.11, 118.06, 116.76, 113.27, 54.30, 23.90. FT-IR (ATR): ν 1695 (C=O), 1638 (C=N), 1501 (C=C), 1238 (C-N) cm^{-1}. HRMS (ESI): *m*/*z* [M−H]$^-$ calcd. for $C_{21}H_{15}N_4O_2$: 355.1201; found: 355.1210.

2-(9-Bromopyrimido[1,2-b]indazol-3-yl)-3,3-dimethyl-3H-indole-5-carboxylic acid (**4b**): Yellow solid. Yield: 70%. mp: >300 °C. ^{1}H NMR (400 MHz, DMSO-d_6): δ = 9.97 (d, 1H, *J* = 1.6 Hz, CHN), 9.53 (d, 1H, *J* = 2.0 Hz, CHN), 8.45 (d, 1H, *J* = 2.0 Hz, Ar-H), 8.14 (s, 1H, Ar-H), 8.01 (dd, 1H, *J* = 6.4, 2.0 Hz, Ar-H), 7.85 (d, 1H, *J* = 9.2 Hz, Ar-H), 7.79 (m, 2H, Ar-H), 1.65 (s, 6H, CH_3). The ^{13}C NMR spectrum could not be measured due to the low solubility. FT-IR (ATR): ν 1675 (C=O), 1636, 1608, (C=N), 1519 (C=C), 1258 (C-N) cm^{-1}. HRMS (ESI): *m*/*z* [M−H]$^-$ calcd. for $C_{21}H_{14}N_4O_2Br$: 433.0300; found: 433.0304.

2-(10-Methoxypyrimido[1,2-b]indazol-3-yl)-3,3-dimethyl-3H-indole-5-carboxylic acid (**4c**): Yellow solid. Yield: 77%. mp: >300 °C. ^{1}H NMR (400 MHz, DMSO-d_6): δ = 9.95 (d, 1H, *J* = 2.0 Hz, CHN), 9.54 (d, 1H, *J* = 2.0 Hz, CHN), 8.18 (d, 1H, *J* = 1.6 Hz, Ar-H), 8.05 (d, 1H, *J* = 7.6, 1.2 Hz, Ar-H), 7.83 (d, 1H, *J* = 8.4 Hz, Ar-H), 7.63 (t, 1H, *J* = 8.4 Hz, Ar-H), 7.41 (d, 1H, *J* = 8.0 Hz, Ar-H), 6.76 (d, 1H, *J* = 7.6 Hz, Ar-H), 4.05 (s, 3H, OCH_3), 1.69 (s, 6H, CH_3). ^{13}C NMR (100 MHz, DMSO-d_6): δ = 182.15 (C=N indole), 167.85 (C=O), 156.33, 155.77, 153.80, 148.32, 146.46, 142.72, 134.43, 132.09, 130.46, 129.33, 123.22, 121.16, 117.35, 108.62, 105.04, 100.29, 56.07, 54.26, 23.91. FT-IR (ATR): ν 1700 (C=O), 1640, 1615 (C=N), 1500 (C=C), 1228 (C-N) cm^{-1}. HRMS (ESI): *m*/*z* [M−H]$^-$ calcd. for $C_{22}H_{17}N_4O_2$: 385.1306; found: 385.1306.

3,3-Dimethyl-2-(8-(trifluoromethyl)pyrimido[1,2-b]indazol-3-yl)-3H-indole-5-carboxylic acid (**4d**): Yellow solid. Yield: 64%. mp: >300 °C. ^{1}H NMR (400 MHz, DMSO-d_6): δ = 10.11 (d, 1H, *J* = 2.0 Hz, CHN), 9.65 (d, 1H, *J* = 2.0 Hz, CHN), 8.56 (d, 1H, *J* = 8.8 Hz, Ar-H), 8.35 (s, 1H, Ar-H), 8.20 (d, 1H, *J* = 1.6 Hz, Ar-H), 8.07 (dd, 1H, *J* = 8.0, 1.2 Hz, Ar-H), 7.86 (d, 1H, *J* = 7.6 Hz, Ar-H), 7.61 (d, 1H, *J* = 8.8 Hz, Ar-H), 1.71 (s, 6H, CH_3). ^{13}C NMR (100 MHz, DMSO-d_6): δ = 181.85 (C=N indole), 167.80 (C=O), 156.17, 150.49, 148.36, 147.59, 143.13, 135.28, 130.98 (q, *J* = 31.5 Hz), 130.45, 129.52, 126.19 (q, *J* = 270.7 Hz), 123.26, 123.21, 121.33, 119.18, 117.11, 114.99 (q, *J* = 4.7 Hz), 114.86, 54.37, 23.75. ^{19}F NMR (376 MHz, DMSO-d_6): δ = -60.75. FT-IR (ATR): ν 1699 (C=O), 1652, 1598 (C=N), 1496 (C=C), 1211 (C-N) cm^{-1}. HRMS (ESI): *m*/*z* [M−H]$^-$ calcd. for $C_{22}H_{14}N_4O_2F_3$: 423.1069; found: 423.1069.

2.5. X-ray Crystallography

X-ray intensity data for yellow crystals of **1b** and **1c** were measured at T = 100 K on a Rigaku/Oxford Diffraction XtaLAB Synergy (Dualflex, AtlasS2) diffractometer (Rigaku Oxford Diffraction, Oxford, UK) fitted with CuKα radiation (λ = 1.54178 Å) so that θ_{max} = 67.7° (corresponding to 100% data completeness). Data reduction, including absorption correction, was accomplished with CrysAlisPro (Oxfordshire, England) [24]. The struc-

tures were solved by direct methods [25] and refined (anisotropic displacement parameters and C-bound H atoms in the riding model approximation) on F^2 [26] A weighting scheme of the form $w = 1/[\sigma^2(F_o^2) + (aP)^2 + bP]$ where $P = (F_o^2 + 2F_c^2)/3$) was introduced towards the end of each refinement. The absolute structure of **1c** was determined based on differences in Friedel pairs included in the data set. The molecular structure diagrams were generated with ORTEP for Windows [27] with 70% displacement ellipsoids, and the packing diagrams were drawn with DIAMOND [28]. Additional data analysis was made with PLATON [29]. Crystal data and refinement details are given in Table 1

Table 1. Crystallographic data and refinement details for **1b** and **1c.**

Compound	1b	1c
Formula	$C_{15}H_9BrN_4$	$C_{16}H_{12}N_4O$
Molecular weight	325.17	276.30
Crystal size/mm^3	0.03 × 0.04 × 0.34	0.03 × 0.07 × 0.31
Colour	yellow	yellow
Crystal system	triclinic	orthorhombic
Space group	$P\bar{1}$	$P2_12_12_1$
a/Å	4.44212(11)	5.35980(8)
b/Å	12.0067(2)	9.27255(15)
c/Å	12.4922(3)	24.9428(4)
a/°	112.154(2)	90
β/°	90.006(2)	90
γ/°	93.8346(19)	90
V/Å^3	615.47(3)	1239.63(3)
Z	2	4
D_c/g cm^{-3}	1.755	1.480
μ/mm^{-1}	4.499	0.788
Measured data	15400	9411
θ range/°	3.8–67.7	3.5–67.7
Unique data	2531	
Observed data ($I \geq 2.0\sigma(I)$)	2420	2476
No. parameters	181	192
R, obs. data; all data	0.027; 0.028	0.028; 0.029
a; b in weighting scheme	0.041; 0.400	0.044; 0.250
R_w, obs. data; all data	0.069; 0.070	0.074; 0.075
Range of residual electron density peaks/eÅ^{-3}	−0.77–0.43	−0.19–0.212

2.6. Computational Details

The Hirshfeld surface analysis was performed using *CrystalExplorer17* (Perth, Australia) [30] based on the methods reported in the literature [31], of which the d_{norm}-map was obtained by calculating the normalised distances from the contact points on the surface to the nearest nucleus inside (d_i) or outside (d_e) the surface upon the adjustment of all X-H bond length to the neutron-derived values [32]. The qualitative energy frameworks were computed for a cluster of 2 × 2 × 3 unit cells with the energy cut-off being set to 8 kJ/mol, using the dispersion corrected CE-B3LYP/DGDZVP model executed through the *Tonto* quantum modelling package [33] integrated in *CrystalExplorer17* [30].

The strength of intermolecular interactions between the molecules was modelled using *NCIPLOT* (Paris, France) [34] by plotting the reduced density gradient as a function of density across the molecules. The computed density derivatives were mapped as isosurfaces which correspond to any favourable or unfavourable interactions as determined by

the sign of the second density Hessian eigenvalue times the density [35]. The VMD Molecular Graphics Viewer (Champaign, USA) [36] was used to visualise the non-covalent interaction indices.

3. Result and Discussion

3.1. Synthesis and Characterisation

As shown in Scheme 2, the condensation reaction of 2-(4-pyridyl)malondialdehyde with 3-aminoindazoles in the presence of acetic acid in refluxing ethanol afforded the corresponding **1a–d** in 55–60% yields. The reaction is more favourable in the presence of a substituent in the 3-aminoindazole substrate, which gives **1b–d** in higher yields compared to that for **1a**.

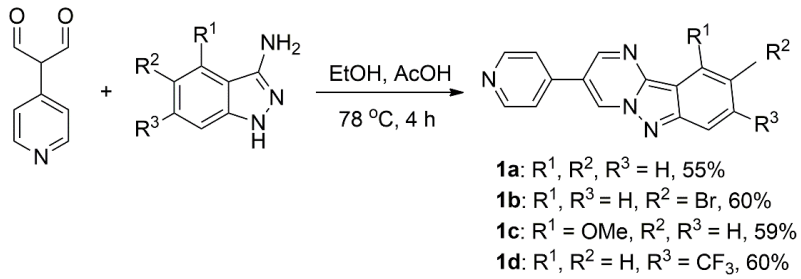

Scheme 2. Synthesis of **1a–d**.

The proposed synthetic mechanism for the formation of **1** is illustrated in Scheme 3, and is based on the assumed condensation reaction. Intermediate **I** is achieved via the mono-condensation reaction between the aldehyde and amino groups. Then, the carbonyl group is protonated to produce intermediate **II**. The nucleophilic attack from the nitrogen atom of the pyrazole to the carbocation centre generates a six-membered ring of intermediate **III**. Next, the deprotonation of the pyrazole ring gives intermediate **IV**. The protonation of a hydroxyl group produces intermediate **V**. Finally, the hydration followed by a deprotonation reaction affords the final product **1**.

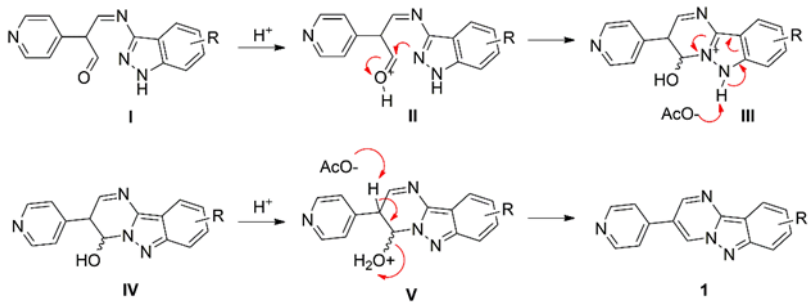

Scheme 3. Proposed mechanism for the formation of **1**.

The ^{1}H NMR spectra of **1a–d** show that the two distinctive pyrimidine olefinic protons appear as doublets (J = 1.6–2.4 Hz) in the range δ 9.21–10.08 ppm, which is consistent with previous findings [23]. The carbon signal of the CF_3 group for **1d** manifests as a quartet (J = 271.2 Hz) at δ 127.56 ppm. The fluorine signal due to the CF_3 group of **1d** is observed at δ −60.57 ppm. In the FT-IR spectra, the typical sp^2 C-H stretching modes of 1a-d are characterised in the range 3036–3060 cm^{-1}, while the peaks between 1102 to 1223 cm^{-1} are attributed to the C–N of the pyrimidine ring.

Subsequently, the synthetic scope of 1,3-dialdehyde substrate was further explored. As illustrated in Scheme 4, precursor **2** was synthesised according to the previous method [37]. The ester hydrolysis reaction of **2** produced **3** in 68% yield. Further, an equimolar condensation reaction of **3** with 3-aminoindazoles generated **4a–d** in 64–85% yields. It was

found that the presence of the electronic substituents on the indazole rings slightly reduces the reaction reactivity which resulted in lower yields of **4b–d** as compared to that of **4a**. The synthetic mechanism for the formation of **4a–d** is presented in the literature [23].

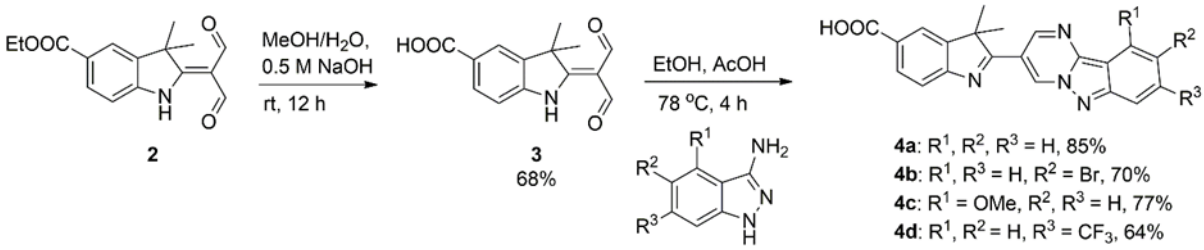

Scheme 4. Synthesis of **4a–d**.

The ^{1}H NMR spectra of **4a–d** reveal that the two olefinic pyrimidine protons resonate between δ 9.47–10.04 ppm as doublets (J = 1.6–2.0 Hz). A singlet signal between δ 1.64–1.66 ppm is assigned to the six methyl protons. Furthermore, the ^{13}C NMR spectra indicate that the most deshielded signals between δ 181.85–182.18 ppm correspond to the C=N(indole) [37], whereas the signals at around δ 167.80 ppm are assigned to the C=O group. The carbon chemical shift of the CF_3 for **4d** appears as a quartet (J = 270.7 Hz) at δ 126.19 ppm. In ^{19}F NMR spectrum of **4d**, the CF_3 signal appeared at δ −60.75 ppm indicating no significant fluorine signal shift is observed when replacing pyridyl with indoleninyl at the C-3 position of the ring. The FT-IR spectra show that the strong intensity bands between ν 1675–1700 cm^{-1} which are ascribed to the stretching mode of the C=O. Moreover, the vibration bands between 1211–1258 cm^{-1} are assigned to the C-N of the pyrimidine ring.

3.2. Crystal and Molecular Structures

Crystals of two representative examples of series **1**, i.e., **1b** and **1c**, were obtained and their structures established by X-ray crystallography. The molecular structures are shown in Figure 1.

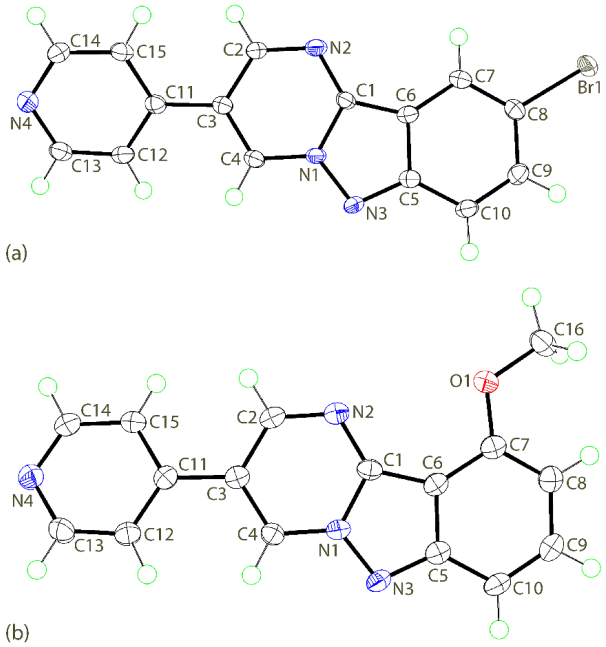

Figure 1. The molecular structures of: (**a**) **1b;** and (**b**) **1c** showing atom labelling schemes and anisotropic displacement parameters at the 70% probability level.

The 13 atoms comprising the pyrimido[1,2-*b*]indazole core of **1b** are strictly co-planar exhibiting a r.m.s. deviation of 0.009 Å with the maximum deviation from the plane being 0.011(2) Å for the C4 atom. Appended to the fused ring system is a 4-pyridyl ring which is twisted out of the plane of the core, as manifested in dihedral angle between the planes of 21.55(8)°. As anticipated, within the five-membered ring, considerable delocalisation of the π-electron density is evident, especially, by the relative shortening of the N1–N3 [1.364(2) Å] and lengthening of the C1–C6 [1.404(3) Å] bonds.

While the molecular structure of **1c** presents similar features to those just described, the r.m.s. deviation for the fused ring system of 0.042 Å is significantly greater than noted for **1b** and is reflected in a dihedral angle of 4.29(8)° between the outer six-membered rings of the pyrimido[1,2-*b*]indazole core, data indicative of a small kink in the molecule. The 4-pyridyl residue forms a dihedral angle of 17.77(6)° with the fused ring system. Despite the aforementioned conformational differences between **1b** and **1c**, the delocalisation of π-electron density is similar. Thus, the N1–N3 [1.3537(18) Å] and C1–C6 [1.406(2) Å] bond lengths follow the same trends established above for **1b**.

The similarity in molecular structures notwithstanding, the molecular packing of **1b** and **1c** present quite distinct features. The unit-cell contents for **1b** are illustrated in Figure 2 with the geometric parameters describing the identified intermolecular contacts included in Table 2. A prominent mode of association between molecules are pyrimidyl-N–H···N(pyrimidyl) interactions leading to six-membered {···NCH}$_2$ synthons. These aggregates stack along the *a*-axis direction and feature π(pyrazolyl)···π(pyrimidyl) contacts between them. An important consequence of these links and the twist between the fused-ring system and the 4-pyridyl group (see above) is that the C4 and C12 atoms of the respective residues are brought into close proximity, these atoms being separated by 3.074(3) Å. Columns are linked into supramolecular layers by type 1 [38,39], Br···N halogen bonding interactions. The layers stack along the *b*-axis without directional interactions between them.

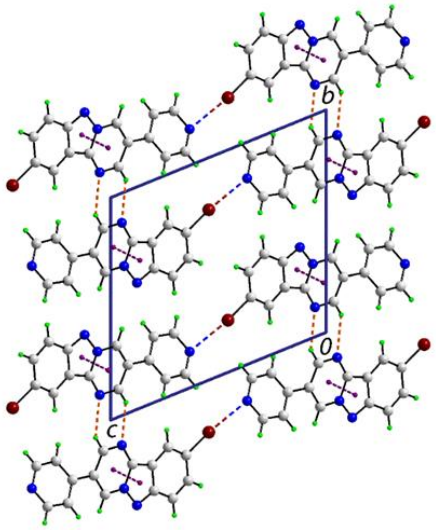

Figure 2. A view of the unit-cell contents for **1b** in projection down the *a*-axis. The C–H···N, Br···N and π···π contacts are shown as orange, blue/brown and purple dashed lines, respectively.

Table 2. Geometric parameters characterising the specified intermolecular contacts for **1b** and **1c**.

A	H	B	H···B	A···B	A–H···B	Symmetry Operation
1b						
C2	H2	N2	2.46	3.298(3)	146	2 + *x*, *y*, 1 + *z*
C8	Br1	N4	1.895(2)	3.0613(19)	171.72(7)	2 + *x*, *y*, 1 + *z*
Cg(N1,N3, C1,C5,C6)	Cg(N1,N2,C1 –C4)	3.4764(11)	0.07(10)	1 + *x*, *y*, *z*		
C4		C12		3.074(3)		1 + *x*, *y*, *z*
1c						
C14	H14	O1	2.44	3.161(2)	133	1 − *x*, ½ + *y*, 1½ − *z*
C4	H4	N3	2.51	3.435(2)	163	½ + *x*, 1½ − *y*, 2 − *z*

The unit-cell contents for **1c** are illustrated in Figure 3 and the intermolecular contacts listed in Table 2. Here, molecules stack along the *a*-axis, being connected by pyrimidyl-C–H···N(pyrazolyl) interactions involving three different molecules in addition to pyridyl-C–H···O(methoxy) interactions within a three-dimensional architecture.

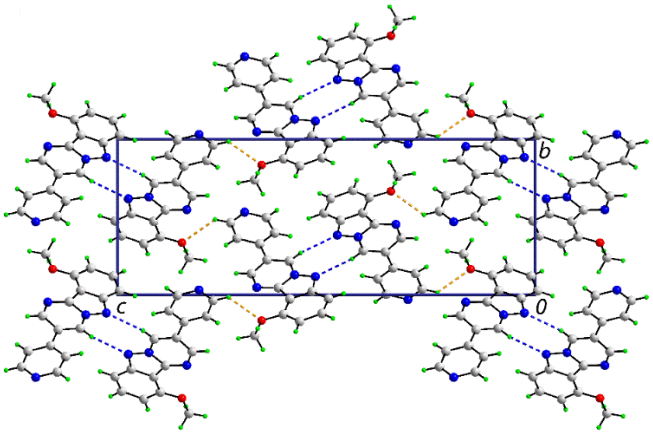

Figure 3. A view of the unit-cell contents for **1c** in projection down the *a*-axis. The C–H···O and C–H···N are shown as orange and blue dashed lines, respectively.

3.3. Computational Chemistry

The X-ray structures of **1b** and **1c** were subjected to Hirshfeld surface analysis to better understand the nature of interactions present in these crystals; see Table 3 for geometric data. As shown in Figure 4, the analysis reveals a number of red spots on the d_{norm}-surfaces indicating the presence of close contacts with distances shorter than the sum of the respective van der Waals radii (∑vdw); the intensity of the spots is directly proportional to the contact distance between the interacting atoms [32]. Owing to the sharing of a common structural framework, **1b** and **1c** exhibit some red spots featuring the same interacting atoms but leading to different contacts as demonstrated by N3···H4 and C13···H10. Among the distinctive contacts in **1b** are Br1···N4 ($\sum d_i + d_e$ = 3.06 Å vs ∑vdw = 3.40 Å), C4···C12 ($\sum d_i + d_e$ = 3.07 Å vs ∑vdw = 3.40 Å) and N2···H2 ($\sum d_i + d_e$ = 2.36 Å vs ∑vdw = 2.64 Å). In **1c**, these include O1···H14 ($\sum d_i + d_e$ = 2.35 Å vs ∑vdw = 2.61 Å).

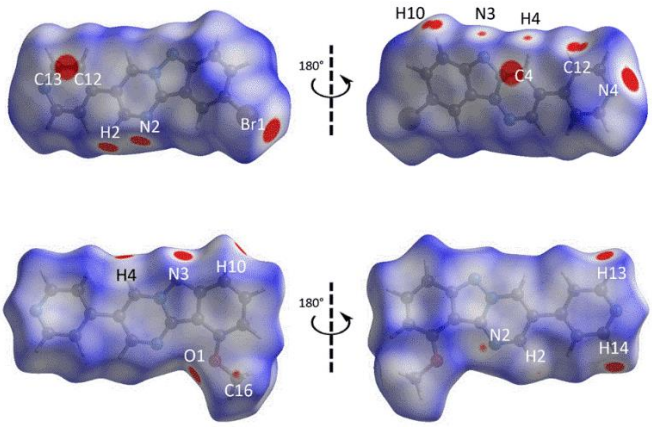

Figure 4. The two views of d_{norm}-surfaces of **1b** (top) and **1c** (bottom), showing the close contacts as indicated by the red spots of variable intensity which are directly proportional to the contact distance (property range: −0.0538 to 1.1022 arbitrary units).

Table 3. List of contact distance between the corresponding red spots as identified on the d_{norm}-surfaces for **1b** and **1c**.

Contact	Distance (Å)	∑vdw(X···Y)	Symmetry Operation
1b			
Br1···N4	3.06	3.40	2 + *x*, *y*, 1 + *z*
N2···H2	2.36	2.64	−1 − *x*, -*y*, −*z*
N3···H4	2.56	2.64	−*x*, 1 − *y*, −*z*
C4···C12	3.07	3.40	1 + *x*, *y*, *z*
C12···H10	2.65	2.79	−*x*, 1 − *y*, −*z*
C13···H10	2.67	2.79	−*x*, 1 − *y*, −*z*
1c			
O1···H14	2.35	2.61	1 − *x*, −½ + *y*, 3/2 − *z*
N4···H2	2.61	2.64	2 − *x*, ½ + *y*, 3/2 − *z*
N3···H4	2.39	2.64	−½ + *x*, 1½ − *y*, 2 − *z*
C13···H10	2.78	2.79	1½ + *x*, 1½ − *y*, 2 − *z*
C1···C8	3.40	3.40	1 + *x*, *y*, *z*
N2···H16c	2.58	2.79	1 + *x*, *y*, *z*

Among those close contacts, only N2···H2 and Cg2(C4)···Cg3(C12) of **1b**, as well as N3···H4, O1···H14 and Cg1(C1)···Cg4(C8) of **1c**, are in line with the PLATON analysis [29], based on geometric criteria, while the rest are identified in the analysis of the calculated Hirshfeld surfaces. Of particular interest is the interaction between Br1 and N4, for which the contact arises from the complementarity between electron-deficient region at the σ-hole [40,41] of Br1 and negatively charge pyridyl-N4 lone-pair of electrons, thereby leading to the charge-induced attraction between the atoms as evident from the electrostatic surface mapping on the Hirshfeld surfaces, Figure 5a. Shape complementarity studies were also conducted for the stacking of the pyrimido[1,2-*b*]indazole fused rings in each of **1b** and **1c** by mapping the curvedness property on the Hirshfeld surface. The mapping reveals that although C4···C12 of **1b** and C1···C8 of **1c** are the only contacts within the aromatic rings having distances shorter than the ∑vdw, the overall fused rings in the respective structure are well stacked as shown in Figure 5b,c which could maximise the configuration entropy and lead to effective entropy-induced attraction for optimum aggregation within the molecules [42].

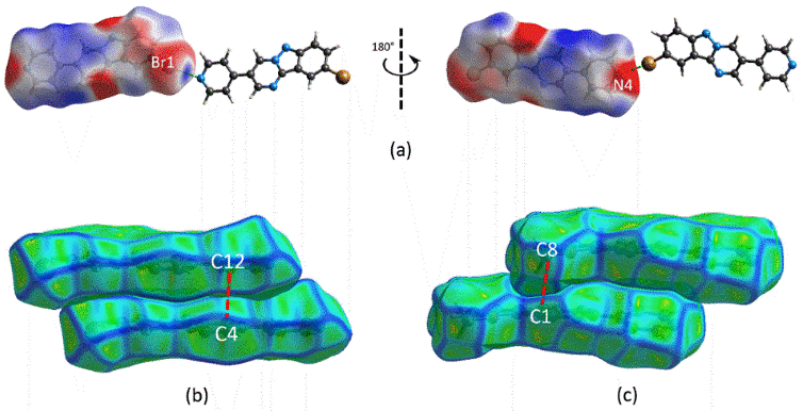

Figure 5. Hirshfeld surfaces mapped with (**a**) electrostatic potential for **1b** (property range: −0.0225 to −0.0528 Hartree atomic units), showing the charge-induced interaction between the electron-deficient site of Br1 at the sigma hole and negative site of the pyridyl ring. Hirshfeld surfaces mapped with curvedness (property range: −4.0 to +0.4 arbitrary units), showing the shape complementarity between the stacking of pyrimido[1,2-*b*]indazole fused rings connected through (**b**) C4···C12 for **1b** and (**c**) C1···C8 for **1c**.

The fingerprint plot analysis was performed to quantify the corresponding close contacts identified through the Hirshfeld surface analysis. The resulting overall fingerprint plots, Figure 6, reveal two essential qualitative observations about the packing in the crystals. Firstly, the analysis affirms the contrast between the packing in **1b** and **1c** as evident from the vastly different paw-like and shield-like profiles, respectively. Secondly, the profile of **1b** is slightly more diffuse in the tail region indicating relatively low packing efficiency as compared to the **1c** counterpart [43], an observation that tallies with the calculated Kitaigorodskii packing index of 73.3% for the former in contrast to 74.8% for the latter [29]. As expected, a comparison of the major common decomposed fingerprint plots delineated into H···H, H···N/N···H, H···C/C···H and C···C contacts shows that the distribution of the corresponding contacts between **1b** and **1c** is different in each case, with the percentage contributions also being distinct, i.e., 31.8, 15.8, 12.0 and 11.5% for **1b** compared to 35.1, 23.2, 22.6 and 7.3% for **1c**. With the exception of H···H contact for **1b**, the remaining major contacts display a tip in their respective profile with $d_i + d_e$ corresponding to the shortest d_{norm}-distance listed in Table 3.

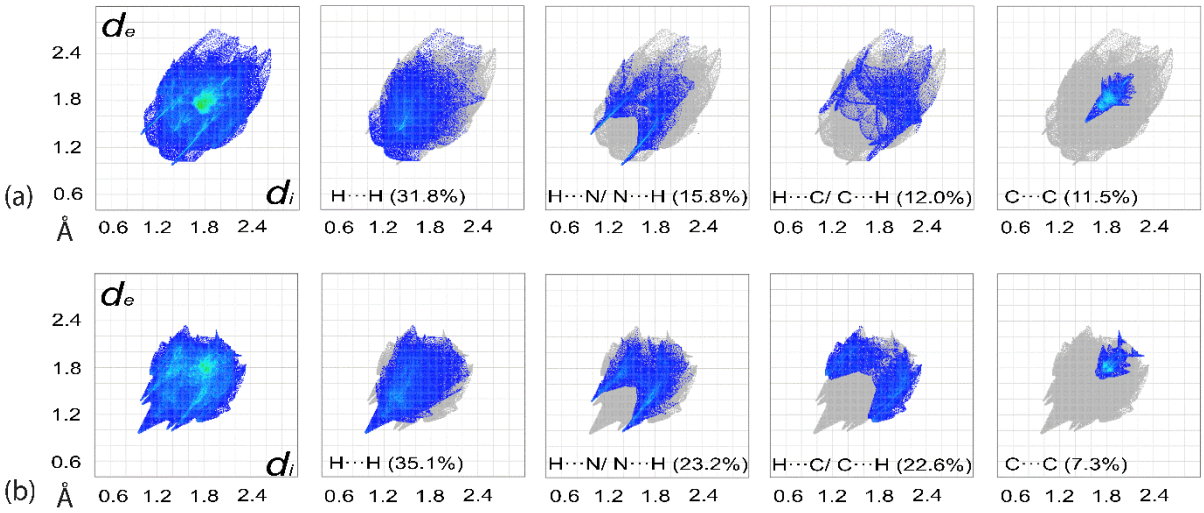

Figure 6. Comparison of the overall and major common decomposed fingerprint plots delineated into H···H, H···N/N···H, H···C/C···H and C···C contacts contacts for (**a**) **1b** and (**b**) **1c**.

The crystals of **1b** and **1c** also display some additional contacts owing to the presence of the Br and O atoms, respectively. Due to the polarisation effect, the Br atom in **1b** tends to participate more in interactions as compared to the O atom in **1c** with the overall contact distribution involving Br being 19.1% which can be delineated into H···Br/Br···H (12.7%), N···Br/Br···N (4.2%), C···Br/Br···C (2.0%) and Br···Br (0.2%). In comparison, O only participates in about 6.5% of the overall contacts which are delineated into H···O/O···H (5.0%), O···C/C···O (0.8%) and O···N/N···O (0.7%) contacts. Among these contacts, only N···Br/Br···N and H···O/O···H have $d_i + d_e$ contact distances less than the respective ∑vdw (cf. Table 1) as revealed through the respective fang-like profiles evident in Figure 7.

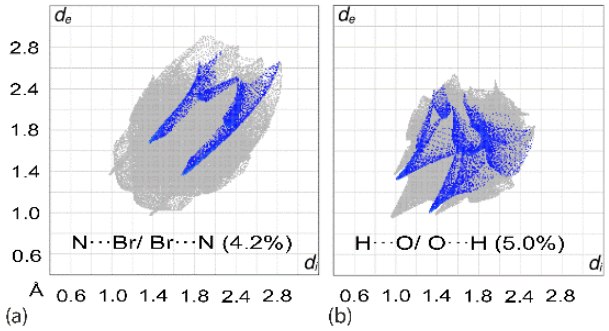

Figure 7. Fingerprint plots decomposed into (**a**) N···Br/Br···N for **1b** and (**b**) H···O/O···H for **1c**.

The enrichment ratios [44] were calculated to establish the propensity for the formation of specific intermolecular interactions in **1b** and **1c**. The calculations show that H···H, H···N/N···H, H···Br/Br···H, C···C, N···C/C···N and N···Br/Br···N contacts of **1b** as well as H···H, H···N/N···H, C···C and H···O/O···H of **1c** have a ratio equal to or greater than unity indicating these contacts are favoured in the molecular packing [44], Figure 8. While the calculated ratios are not exactly in line with the trends of $d_i + d_e$ distances, in particular for H···H, H···Br/Br···H and N···C/C···N in **1b**, these contacts have been established to play an essential role in the molecular packing.

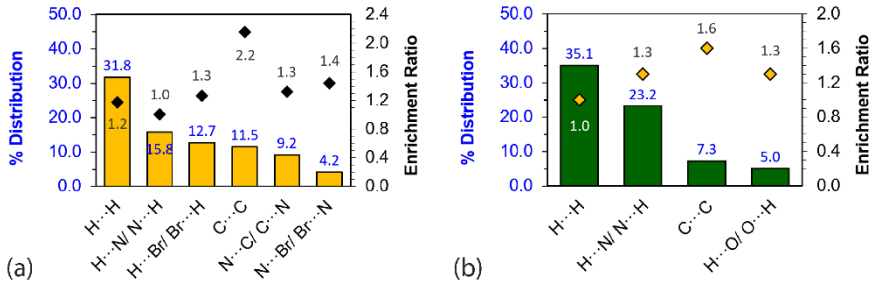

Figure 8. The calculated enrichment ratios (diamonds) greater than unity for selected contacts and their percentage distribution (bars) in (**a**) **1b** and (**b**) **1c**.

Having established the close contacts through the Hirshfeld surface analysis, all pairwise interactions were subjected to interaction energy calculations to evaluate the strength of specific contacts in the respective crystals. In the absence of conventional hydrogen bonding in the crystal, the most stable interaction in **1b** arises from the π···π interaction involving N1–C1–N2–C2–C3–C4 (Cg2) and N4–C13–C12–C11–C15–C14 (Cg3) with the total interaction energy for this contact, E_{int}, being −60.1 kJ/mol (Table 4) mainly owing to the effective stacking between the fused rings as discussed above. This is followed by the eight-membered {···NNCH}$_2$ homosynthon complemented by C10–H10···C12 and C10–H10···C13 interactions with a combined E_{int} of −41.4 kJ/mol. The halogen bonding contact arising from C8–Br1···N4 results in the smallest E_{int} of −8.1 kJ/mol.

Table 4. Interaction energies (kJ/mol) for all close contacts present in the crystals of **1b** and **1c** [a].

Close Contact	$E_{electrostatic}$	$E_{polarization}$	$E_{dispersion}$	$E_{repulsion}$	E_{int}	Symmetry Operation
1b						
Cg2(C4)···Cg3(C12)	−39.9	−2.9	−91.4	103.3	−60.1	1 + x, *y*, *z*
C4–H4···N3 (×2) + C10–H10···C12 (×2) + C10–H10···C13 (×2)	−34.6	−5.9	−34.7	48.1	−41.4	−*x*, 1 − *y*, −*z*
C2–H2···N2 (×2)	−28.3	−5.0	−30.2	42.3	−33.8	−1 − *x*, −*y*, −*z*
C8–Br1···N4	−15.3	−1.7	−8.1	26.4	−8.1	2 + *x*, *y*, 1 + *z*
1c						
Cg1(C1)···Cg4(C8) + C16–H16c···N2	H14	O1	2.44	3.161(2)	133	1 − *x*, ½ + *y*, 1½ − *z*
C14–H14···O1	−19.3	−4.6	−19.5	26.1	−24.6	1 − *x*, ½ + *y*, 1½−*z*
C4–H4···N3	−14.7	−4.2	−19.7	22.1	−22.2	½ + *x*, 1½ − *y*, 2 − *z*
C2–H2···N4	−10.5	−2.2	−13.3	12.2	−16.8	2 − *x*, ½ + *y*, 1½ − *z*
C10–H10···C13	−3.3	−1.0	−11.4	14.4	−5.3	−1½ + *x*, 1½ − *y*, 2 − *z*

[a] Cg1 = N1–N3–C5–C6–C1; Cg2 = N1–C1–N2–C2–C3–C4; Cg3 = N4–C13–C12–C11–C15–C14; Cg4 = C5–C6–C7–C8–C9–C10.

In **1c**, the π···π contacts involving N1–N3–C5–C6–C1 (Cg1) and C5–C6–C7–C8–C9–C10 (Cg4) results in an almost equivalent E_{int} of −59.3 kJ/mol relative to **1b**, although it is noted that the π···π contacts are complemented by the C16–H16c···N2 contact identified through the Hirshfeld surface analysis. Other contacts contribute to stabilisation of the packing to a lesser extent with E_{int} ranging from −24.6 to −5.3 kJ/mol, respectively.

The non-covalent interaction (NCI) plots were calculated to complement the energy calculations for interactions involving the fused rings as well as the halogen bonding contact between Br1 and N4. As shown in Figure 9, a large isosurface derived from the reduced density gradient [35] is seen to be extended across the entire stacked molecules in **1b** while a relatively smaller isosurface is observed across the fused rings in **1c**, both indicating significant attractive forces existing between the molecules. By contrast, a clearly smaller isosurface is found between the Br1 and N4 atomds indicating a weak but attractive force for the halogen bonding contact. Overall, the results from NCI plot complement the computed interaction energies for the respective close contacts.

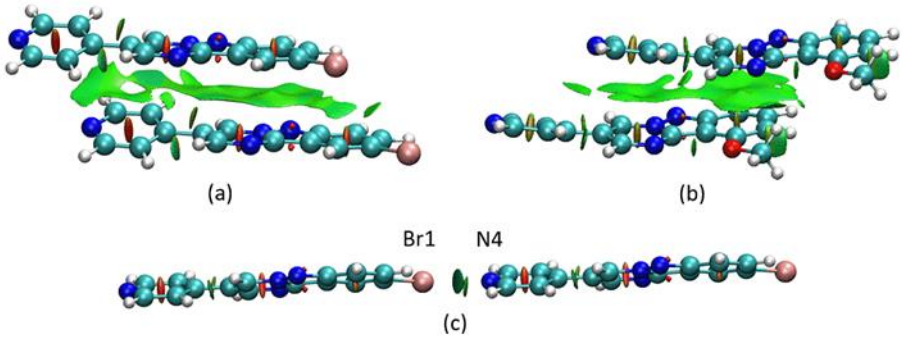

Figure 9. NCI plots (isovalue = 0.5 a.u.) showing the interaction between (**a**) the fused aromatic rings of **1b**, (**b**) the fused aromatic rings of **1a** and (**c**) Br1 and N4 for **1b**.

A simulation of energy frameworks was conducted for **1b** and **1c** to assess the nature of the forces characterising the interactions and their influence upon the molecular packing. Overall, the packing of **1b** and **1c** are mainly sustained by dispersion forces attributed to π···π interactions between the fused aromatic rings supported by relatively weaker C–H···N interactions, in which the combined forces lead to a ladder-like dispersion energy framework in **1b**, while a beta sheet-like framework is observed in **1c**, Figure 10. The same

interactions also contributed to the electrostatic forces but to a lesser extent. For **1b**, peripheral electrostatic forces arising from the Br···N halogen bonding contact is observed that strengthens the electrostatic energy framework and which subsequently inherited by the total energy framework. As for **1c**, the electrostatic forces are mainly contributed by π···π and C–H···O interactions that lead to a tile-like energy framework, while the total energy framework remains very much the same as the dispersion energy framework.

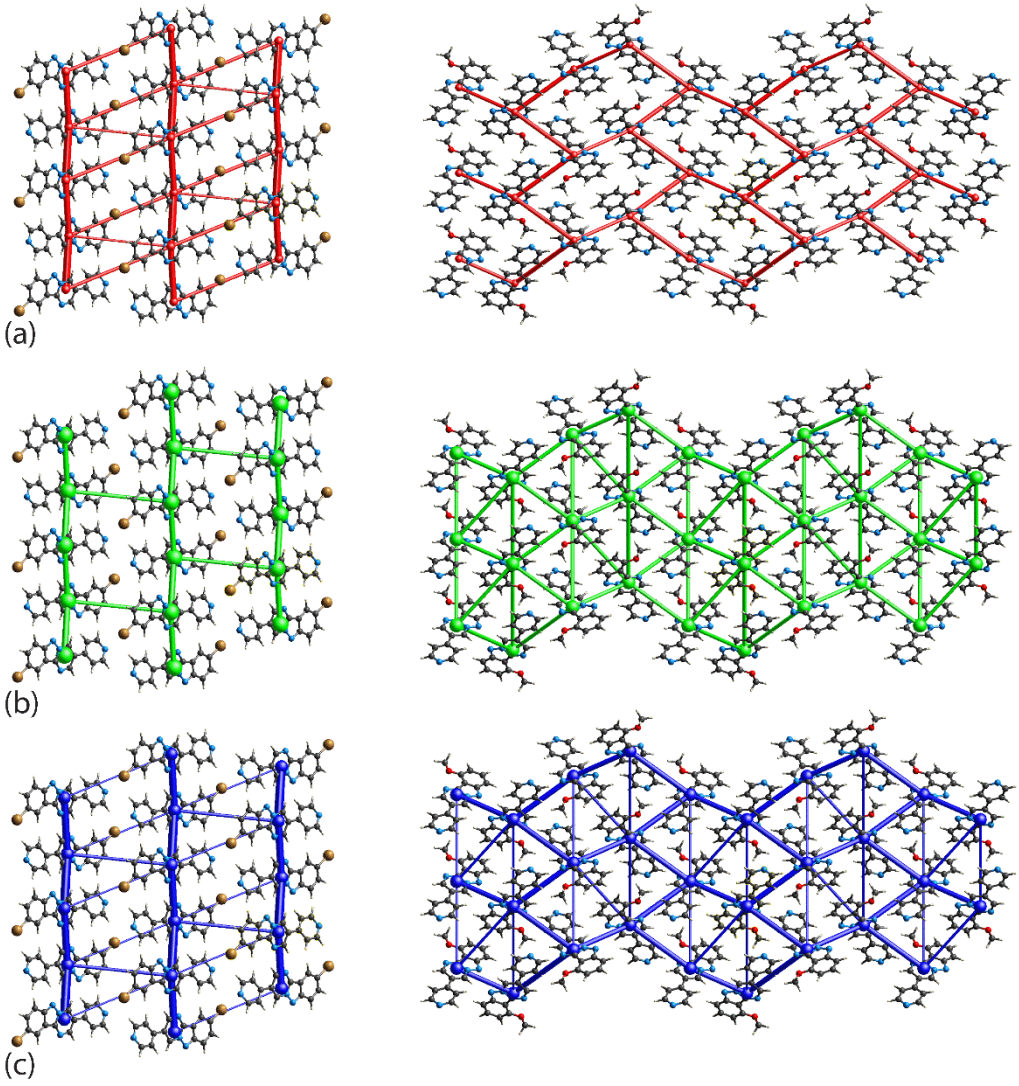

Figure 10. Perspective views of the (**a**) electrostatic energy; and (**b**) dispersion force and (**c**) overall energy frameworks for **1b** (left) and **1c** (right). The cylindrical radius is proportional to the relative strength of the corresponding energies. and they were adjusted to the same scale factor of 100 with a cut-off value of 8 kJ/mol within a 2 × 2 × 3 unit cells.

4. Conclusions

In conclusion, the synthesis of substituted pyrimido[1,2-*b*]indazoles via a straightforward condensation reaction between the 1,3-dialdehydes and 3-aminoindazoles was accomplished. This synthetic approach offers several advantages such as economic, operationally simple and showed functional groups tolerance with different substituents on both substrates. X-ray crystallography on representative examples support the spectroscopic assignments and indicate substantial π-electron density delocalisation over the fused ring system.

Supplementary Materials: The following supporting information can be downloaded at: https://www.mdpi.com/article/10.3390/cryst12091283/s1. Figures S1–S19 contain ^{1}H, $^{13}C\{^{1}H\}$ and ^{19}F NMR spectra of **1a–d**, **3** and **4a–d**.

Author Contributions: Investigation, formal analysis, writing—original draft preparation, review and editing, A.Q.R., S.L.T. and E.R.T.T. All authors have read and agreed to the published version of the manuscript.

Funding: This research was partially funded by Sunway University Sdn Bhd, grant number GRTIN-RRO-56-2022.

Institutional Review Board Statement: Not applicable.

Informed Consent Statement: Not applicable.

Data Availability Statement: Crystallographic datasets for the structures **1b** and **1c** are available through the Cambridge Structural Database with deposition numbers CCDC 2116839 (**1b**) and 2116843 (**1c**). These data can be obtained free of charge via https://www.ccdc.cam.ac.uk/structures/ (accessed on 30 July 2022).

Acknowledgments: A.Q. Ramle would like to thank the Universiti Sains Malaysia for providing the lecturer scheme opportunity and research facilities.

Conflicts of Interest: The authors declare no conflicts of interest.

References

1. Balwe, S.G.; Jeong, Y.T. An approach towards the synthesis of novel fused nitrogen tricyclic heterocyclic scaffolds via GBB reaction. *Org. Biomol. Chem*. **2018**, *16*, 1287–1296. https://doi.org/10.1039/C7OB02933K.
2. Gao, Q.; Han, X.; Tong, P.; Zhang, Z.; Shen, H.; Guo, Y.; Bai, S. Aerobic α,β-C(sp^3)–H bond difunctionalization and C–N bond cleavage of triethylamine: Difunctional ammonium iodide enabling the regioselective synthesis of 4-arylpyrimido[1,2-*b*]indazoles. *Org. Lett.* **2019**, *21*, 6074–6078. https://doi.org/10.1021/acs.orglett.9b02218.
3. Yakaiah, T.; Kurumurthy, C.; Lingaiah, B.P.V.; Narsaiah, B.; Pamanji, R.; Velatooru, L.R.; Rao, J.V.; Gururaj, S.; Parthasarathy, T.; Sridhar, B. $GdCl_3$ promoted synthesis of novel pyrimidine fused indazole derivatives and their anticancer activity. *Med. Chem. Res*. **2012**, *21*, 4261–4273. https://doi.org/10.1007/s00044-011-9962-0.
4. Bharate, S.B.; Mahajan, T.R.; Gole, Y.R.; Nambiar, M.; Matan, T.T.; Kulkarni-Almeida, A.; Balachandran, S.; Junjappa, H.; Balakrishnan, A.; Vishwakarma, R.A. Synthesis and evaluation of pyrazolo[3,4-*b*]pyridines and its structural analogues as TNF-α and IL-6 inhibitors. *Bioorg. Med. Chem*. **2008**, *16*, 7167–7176. https://doi.org/10.1016/j.bmc.2008.06.042.
5. Jismy, B.; El Qami, A.; Pišlar, A.; Frlan, R.; Kos, J.; Gobec, S.; Knez, D.; Abarbri, M. Pyrimido[1,2-*b*]indazole derivatives: Selective inhibitors of human monoamine oxidase B with neuroprotective activity. *Eur. J. Med. Chem*. **2021**, *209*, 112911. https://doi.org/10.1016/j.ejmech.2020.112911.
6. Chino, A.; Seo, R.; Amano, Y.; Namatame, I.; Hamaguchi, W.; Honbou, K.; Mihara, T.; Yamazaki, M.; Tomishima, M.; Masuda, N. Fragment-based discovery of pyrimido[1,2-*b*] indazole PDE10A inhibitors. *Chem. Pharm. Bull*. **2018**, *66*, 286–294. https://doi.org/10.1248/cpb.c17-00836.
7. Han, X.; Pin, S.S.; Burris, K.; Fung, L.K.; Huang, S.; Taber, M.T.; Zhang, J.; Dubowchik, G.M. Synthesis and structure–activity relationship of imidazo[1,2-*a*]benzimidazoles as corticotropin-releasing factor 1 receptor antagonists. *Bioorg. Med. Chem. Lett*. **2005**, *15*, 4029–4032. https://doi.org/10.1016/j.bmcl.2005.06.028.
8. Ndakala, A.J.; Gessner, R.K.; Gitari, P.W.; October, N.; White, K.L.; Hudson, A.; Fakorede, F.; Shackleford, D.M.; Kaiser, M.; Yeates, C.; et al. Antimalarial Pyrido[1,2-*a*]benzimidazoles. *J. Med. Chem*. **2011**, *54*, 4581–4589. https://doi.org/10.1021/jm200227r.
9. Yakaiah, T.; Lingaiah, B.P.V.; Narsaiah, B.; Kumar, K.P.; Murthy, U.S.N. $GdCl_3$ catalysed Grieco condensation: A facile approach for the synthesis of novel pyrimidine and annulated pyrimidine fused indazole derivatives in single pot under mild conditions and their anti-microbial activity. *Eur. J. Med. Chem*. **2008**, *43*, 341–347. https://doi.org/10.1016/j.ejmech.2007.03.031.
10. Li, L.; Xu, H.; Dai, L.; Xi, J.; Gao, L.; Rong, L. An efficient metal-free cascade process for the synthesis of 4-arylpyrimido[1,2-*b*]indazole-3-carbonitrile derivatives. *Tetrahedron* **2017**, *73*, 5358–5365. https://doi.org/10.1016/j.tet.2017.07.035.
11. Palaniraja, J.; Roopan, S.M.; Rayalu, G.M. One-pot synthesis of highly functionalized pyrimido[1,2-*b*]indazoles via 6-endo-dig cyclization. *RSC Adv.* **2016**, *6*, 24610–24616. https://doi.org/10.1039/C6RA02596J.
12. Liu, X.; Zhou, J.; Lin, J.; Zhang, Z.; Wu, S.; He, Q.; Cao, H. Controllable site-selective construction of 2- and 4-substituted pyrimido[1,2-*b*]indazole from 3-aminoindazoles and ynals. *J. Org. Chem*. **2021**, *86*, 9107–9116. https://doi.org/10.1021/acs.joc.1c01094.
13. Jadhav, A.M.; Balwe, S.G.; Lim, K.T.; Jeong, Y.T. A novel three-component method for the synthesis of spiro[chromeno [4′,3′:4,5] pyrimido[1,2-*b*] indazole-7,3′-indoline]-2′,6(9*H*)-dione. *Tetrahedron* **2017**, *73*, 2806–2813. https://doi.org/10.1016/j.tet.2017.03.084.
14. Jadhav, A.M.; Balwe, S.G.; Jeong, Y.T. An efficient protocol for synthesis of novel polyheterocyclic chromeno pyrimido[1,2-*b*]indazolone derivatives using $[Et_3NH][HSO_4]$ as a reusable catalyst under solvent-free conditions. *Tetrahedron Lett*. **2019**, *60*, 151251. https://doi.org/10.1016/j.tetlet.2019.151251.

15. Zhou, Y.; Lou, Y.; Wang, Y.; Song, Q. Oxidant-controlled divergent transformations of 3-aminoindazoles for the synthesis of pyrimido[1,2-*b*]-indazoles and aromatic nitrile-derived dithioacetals. *Org. Chem. Front*. **2019**, *6*, 3355–3359. https://doi.org/10.1039/C9QO00847K.
16. Balwe, S.G.; Shinde, V.V.; Rokade, A.A.; Park, S.S.; Jeong, Y.T. Green synthesis and characterization of silver nanoparticles (Ag NPs) from extract of plant Radix Puerariae: An efficient and recyclable catalyst for the construction of pyrimido[1,2-*b*]indazole derivatives under solvent-free conditions. *Catal. Commun*. **2017**, *99*, 121–126. https://doi.org/10.1016/j.catcom.2017.06.006.
17. Kong, W.; Zhou, Y.; Song, Q. Lewis-acid promoted chemoselective condensation of 2-aminobenzimidazoles or 3-aminoindazoles with 3-ethoxycyclobutanones to construct fused nitrogen heterocycles. *Adv. Synth. Catal.* **2018**, *360*, 1943–1948. https://doi.org/10.1002/adsc.201701641.
18. Palaniraja, J.; Roopan, S.M.; Rayalu, G.M.; Al-Dhabi, N.A.; Arasu, M.V. A metal-free regioselective multicomponent approach for the synthesis of free radical scavenging pyrimido-fused indazoles and their fluorescence studies. *Molecules* **2016**, *21*, 1571. https://doi.org/10.3390/molecules21111571.
19. Annareddygari, S.; Kasireddy, V.R.; Reddy, J. Transition-metal-free N-arylation: A general approach to aza-fused poly-heteroaromatics. *J. Heterocycl. Chem*. **2019**, *56*, 3267–3276. https://doi.org/10.1002/jhet.3722.
20. Volovenko, Y.M.; Chuiguk, V.A. Pyrimido[1,2-*b*]indazoles from 3-aminoindazoles and *β*-diketones. *Chem. Heterocycl. Compd*. **1974**, *10*, 859–860. https://doi.org/10.1007/BF00471374.
21. Geng, X.; Xu, Z.; Cai, Y.; Wang, L. Visible-light-driven multicomponent cyclization by trapping a 1,3-vinylimine ion intermediate: A direct approach to pyrimido[1,2-*b*]indazole derivatives. *Org. Lett*. **2021**, *23*, 8343–8347. https://doi.org/10.1021/acs.orglett.1c03076.
22. Zhou, J.; Li, W.; Zheng, H.; Pei, Y.; Liu, X.; Cao, H. Visible light-induced cascade cyclization of 3-aminoindazoles, ynals, and chalcogens: Access to chalcogen-containing pyrimido[1,2-*b*]-indazoles. *Org. Lett*. **2021**, *23*, 2754–2759. https://doi.org/10.1021/acs.orglett.1c00664.
23. Ramle, A.Q.; Fei, C.C.; Tiekink, E.R.T.; Basirun, W.J. Indoleninyl-substituted pyrimido[1,2-*b*]indazoles *via* a facile condensation reaction. *RSC Adv*. **2021**, *11*, 24647–24651. https://doi.org/10.1039/D1RA04372B.
24. *Rigaku Oxford Diffraction; CrysAlis PRO*; Rigaku Oxford Diffraction: Oxfordshire, UK, 2017.
25. Sheldrick, G.M. A short history of SHELX. *Acta Crystallogr. Sect. A: Found. Crystallogr*. **2008**, *64*, 112–122. https://doi.org/10.1107/S0108767307043930.
26. Sheldrick, G.M. Crystal structure refinement with SHELXL. *Acta Crystallogr. Sect. C: Struct. Chem*. **2015**, *71*, 3–8. https://doi.org/10.1107/S2053229614024218.
27. Farrugia, L.J. WinGX and ORTEP for Windows: An update. *J. Appl. Crystallogr*. **2012**, *45*, 849–854. https://doi.org/10.1107/S0021889812029111.
28. Brandenburg, K. *DIAMOND*; Crystal Impact GbR: Bonn, Germany, 2006.
29. Spek, A.L. checkCIF validation ALERTS: What they mean and how to respond. *Acta Crystallogr. Sect. E: Crystallogr. Commun*. **2020**, *76*, 1–11. https://doi.org/10.1107/S2056989019016244.
30. Spackman, P.R.; Turner, M.J.; McKinnon, J.J.; Wolff, S.K.; Grimwood, D.J.; Jayatilaka, D.; Spackman, M.A. CrystalExplorer: A program for Hirshfeld surface analysis, visualization and quantitative analysis of molecular crystals. *J. Appl. Crystallogr.* **2021**, *54*, 1006–1011. https://doi.org/10.1107/S1600576721002910.
31. Tan, S.L.; Jotani, M.M.; Tiekink, E.R.T. Utilizing Hirshfeld surface calculations, non-covalent interaction (NCI) plots and the calculation of interaction energies in the analysis of molecular packing. *Acta Crystallogr. Sect. E: Crystallogr. Commun*. **2019**, *75*, 308–318. https://doi.org/10.1107/S2056989019001129.
32. Spackman, M.A.; Jayatilaka, D. Hirshfeld surface analysis. *CrystEngComm* **2009**, *11*, 19–32. https://doi.org/10.1039/B818330A.
33. Jayatilaka, D.; Grimwood, D.J. *Tonto: A Fortran Based Object-Oriented System for Quantum Chemistry and Crystallography*; Springer: Berlin/Heidelberg, Germany, 2003; pp. 142–151.
34. Contreras-García, J.; Johnson, E.R.; Keinan, S.; Chaudret, R.; Piquemal, J.-P.; Beratan, D.N.; Yang, W. NCIPLOT: A program for plotting noncovalent interaction regions. *J. Chem. Theory Comput*. **2011**, *7*, 625–632. https://doi.org/10.1021/ct100641a.
35. Johnson, E.R.; Keinan, S.; Mori-Sánchez, P.; Contreras-García, J.; Cohen, A.J.; Yang, W. Revealing noncovalent interactions. *J. Am. Chem. Soc*. **2010**, *132*, 6498–6506. https://doi.org/10.1021/ja100936w.
36. Humphrey, W.; Dalke, A.; Schulten, K. VMD: Visual molecular dynamics. *J. Mol. Graph*. **1996**, *14*, 33–38. https://doi.org/10.1016/0263-7855(96)00018-5.
37. Ramle, A.Q.; Khaledi, H.; Hashim, A.H.; Mingsukang, M.A.; Mohd Arof, A.K.; Ali, H.M.; Basirun, W.J. Indolenine—dibenzotetraaza [14] annulene Ni (II) complexes as sensitizers for dye—sensitized solar cells. *Dyes Pigm*. **2019**, *164*, 112–118.
38. Sakurai, T.; Sundaralingam, M.; Jeffrey, G.A. A nuclear quadrupole resonance and x-ray study of crystal structure of 2,5-dichloroaniline. *Acta Crystallogr*. **1963**, *16*, 354–363. https://doi.org/10.1107/S0365110X63000979.
39. Desiraju, G.R.; Parthasarathy, R. The nature of halogen...halogen interactions—are short halogen contacts due to specific attractive forces or due to close packing of nonspherical atoms. *J. Am. Chem. Soc*. **1989**, *111*, 8725–8726. https://doi.org/10.1021/ja00205a027.
40. Clark, T.; Hennemann, M.; Murray, J.S.; Politzer, P. Halogen bonding: The sigma-hole. *J. Mol. Model*. **2007**, *13*, 291–296. https://doi.org/10.1007/s00894-006-0130-2.
41. Murray, J.S.; Politzer, P. Interaction and polarization energy relationships in *σ*-hole and *π*-hole bond. *Crystals* **2020**, *10*, 76. https://doi.org/10.3390/cryst10020076.

42. Li, Y.; Zhang, X.; Cao, D. The Role of Shape Complementarity in the Protein-Protein Interactions. *Sci. Rep*. **2013**, *3*, 3271. https://doi.org/10.1038/srep03271.
43. Lee, S.M.; Lo, K.M.; Tan, S.L.; Tiekink, E.R.T. (Tris{2-[(5-chloro-2-oxidobenzylidene-κ*O*)amino-κ*N*]ethyl}amine-κ*N*)ytterbium(III): Crystal structure and Hirshfeld surface analysis. *Acta Crystallogr. Sect. E: Crystallogr. Commun*. **2016**, *72*, 1390–1395. https://doi.org/10.1107/S2056989016013748.
44. Jelsch, C.; Ejsmont, K.; Huder, L. The enrichment ratio of atomic contacts in crystals, an indicator derived from the Hirshfeld surface analysis. *IUCrJ* **2014**, *1*, 119–128. https://doi.org/10.1107/S2052252514003327.